Droplet migration into dead-end channels at high salinity enhanced by micelle gradients of a zwitterionic surfactant

Nan Shi* and Amr Abdel-Fattah
EXPEC-ARC, Saudi Aramco, Dhahran 31311, Saudi Arabia

(Received 2 November 2020; revised 21 December 2020; accepted 13 May 2021; published 28 May 2021)

Direct microscopic visualization experiments are reported to quantify the diffusiophoretic migration of oil droplets in high-salinity solutions ($c > 0.7$ mol/L). Contrary to usual results in the low-salinity limit, we find negligible enhancement in the droplet migration under electrolyte gradients at high salinity. Rationalization of this observation suggests nonelectrolyte gradients as possible alternatives to effectively drive diffusiophoresis beyond the low-salinity limit. In particular, micelle gradients of the zwitterionic surfactant clearly enhance droplet migration into dead-end channels at high salinity. Characterization of such migration—proceeding down the gradient—indicates repulsive interaction between micelles and droplets, which may involve various micelle dynamics at different salinity conditions. Furthermore, we identify a synergistic effect from simultaneous electrolyte and micelle gradients to further enhance droplet migration. These findings, together with the robustness of our experimental system, contribute knowledge or enable more studies to understand and design colloid migration in varieties of systems at elevated salinity.

DOI: 10.1103/PhysRevFluids.6.053103

I. INTRODUCTION

Diffusiophoresis (DP) is the autonomous and directed migration of colloidal particles under ambient chemical gradients [1–3]. As nonuniform solute concentration is generated rather ubiquitously by many physical, chemical, and biological processes [4], DP has received increasing attention for understanding and designing colloidal dynamics in various contexts. Examples include film deposition of latex particles [3,5], membrane fouling [6,7], and filtration, trapping or focusing of particles [8–11]. In particular, studies have shown that DP can enhance both inward and outward transport of particles in the dead-end pore geometry [12,13], and suggested applications of such phenomena for enhanced oil recovery [14] and laundry detergent cleaning [15].

Noticeably, most of these studies focus on the classic DP phenomenon, where the migration of charged colloids is driven by electrolyte gradients in the low-salinity limit ($c < 100$ mM). On the other hand, many natural and synthetic systems involve high-salinity conditions, such as seawater ($c \approx 1$ M), wastewater in reverse osmosis ($c \approx 2$ M) [16], and geological reservoirs ($c > 2$ M) [17,18]. Understanding and designing colloid migration in these systems requires knowledge of DP beyond the low-salinity limit. Compared with the availability of theoretical work [19–21], experimental studies of DP at high salinity are limited by the difficulty of finding stable colloidal systems at such conditions. Thus far, DP at elevated salinity has only been observed under NaCl gradients and measured indirectly [17].

*nan_shi@ucsb.edu

Here, we utilize a robust experimental system to study DP migration of mineral oil droplets in high-salinity solutions. The zwitterionic surfactant CBS (cocamidopropyl hydroxysultaine, Colonial Chemical) produces stable oil-in-water emulsions in synthetic seawater (SW, $c \approx 0.7$ M) and connate water (CW, $c \approx 2.5$ M) [22]. And the microfluidic device establishes transient chemical gradients in dead-end channels formed *in situ*. Altogether our system enables direct visualization to quantify DP migration in such high-salinity solutions.

Our results show that electrolyte gradients at high salinity could not effectively drive DP as they usually do in the low-salinity limit. We rationalize this observation by discussing droplets' zeta potential and the scaling of DP velocity in our system. The analysis further suggests nonelectrolyte gradients as possible alternatives for driving DP beyond the low-salinity limit. Specifically, we observe DP migration that proceeds *down* CBS micelle gradients, leading to enhanced droplet transport in dead-end channels. Unique system properties suggest a different surfactant-colloid interaction from well-known examples, such as electrostatics [15,23–25], solute-capillary flow [26,27], and micelle solubilization [28]. Instead, we propose a repulsive micelle-droplet interaction based on which a transport model is developed to understand DP migration under CBS gradients. Finally, when both micelle and electrolyte gradients exist, droplets migrate deeper into the dead-end channel compared with experiments involving either gradients. Possible changes of the micelle structure with ionic compositions are discussed to explain the synergistic effect of multiple chemical gradients.

II. METHODS

To establish transient chemical gradients and directly visualize droplet migration in a convection-free environment, we design a microfluidic device that enables *in situ* formation of dead-ends [Fig. 1(a), see Supplemental Material for details [29]]. Polymerization of the photocurable glue, Norland Optical Adhesive 81 (NOA-81), blocks one end of the three horizontal channels and turns them into dead-end channels [Fig. 1(b)]. By designing solution 1 that initially fills the microfluidic device and solution 2 that continuously flows in the main channel, diffusion of solute species into or out of dead-end channels generates transient gradients that are directed outward or inward, respectively [Fig. 1(c)]. Such a gradient is visualized by the diffusion of a fluorescent dye into the dead-end channel [Fig. 1(d)], where solution 1 is DI water and solution 2 is the fluorescein solution (0.5 mg/mL). Without convection, fluorescein concentration in the dead-end channel would follow

$$c/c_0 = 1 - \mathrm{erf}(x/\sqrt{4Dt}), \tag{1}$$

which describes diffusion in a semi-infinite space [30]. Fitting measured intensity profiles with Eq. (1) [Fig. 1(e)] yields $D \approx 350\ \mu\mathrm{m}^2/\mathrm{s}$ for the diffusion coefficient of fluorescein and $L_0 \approx 150\ \mu\mathrm{m}$ for the penetration depth of convective flow streamlines into the dead-end channel, both consistent with reported values [31,32]. We also use the fit diffusion coefficient ($D = 350\ \mu\mathrm{m}^2/\mathrm{s}$) and duration of the experiment ($t = 30$ min) to justify the assumption of diffusion in semi-infinite space, where the estimated diffusion distance $\sqrt{4Dt} \approx 1.6$ mm is indeed much less than the total length of the dead-end channel (≈6 mm) in our microfluidic device.

Using this microfluidic device, we study the migration of mineral oil droplets (dispersed in solution 2 at 0.5% v/v) into the dead-end channel driven by different chemical gradients at high salinity. By labeling droplets with the hydrophobic fluorescent dye Nile Red (0.5 mg/mL), their migration can be visualized and quantified based on the change of fluorescence intensity profiles in the dead-end channel (see Supplemental Material for details [29]). Because each experiment of observing droplet migration lasts for 10 hours, it is necessary to minimize the photobleaching effect on measuring droplet migration. Indeed, in our gradient-visualization experiments, fluorescein molecules are continuously exposed to the excitation light for 30 min, and this long exposure time leads to lower fluorescent intensity than the prediction by Eq. (1) [Fig. 1(e)]. Although Nile Red has been reported to resist photobleaching better than fluorescein [33], we further automate the experimental system such that the microfluidic channel is only exposed to the excitation light when

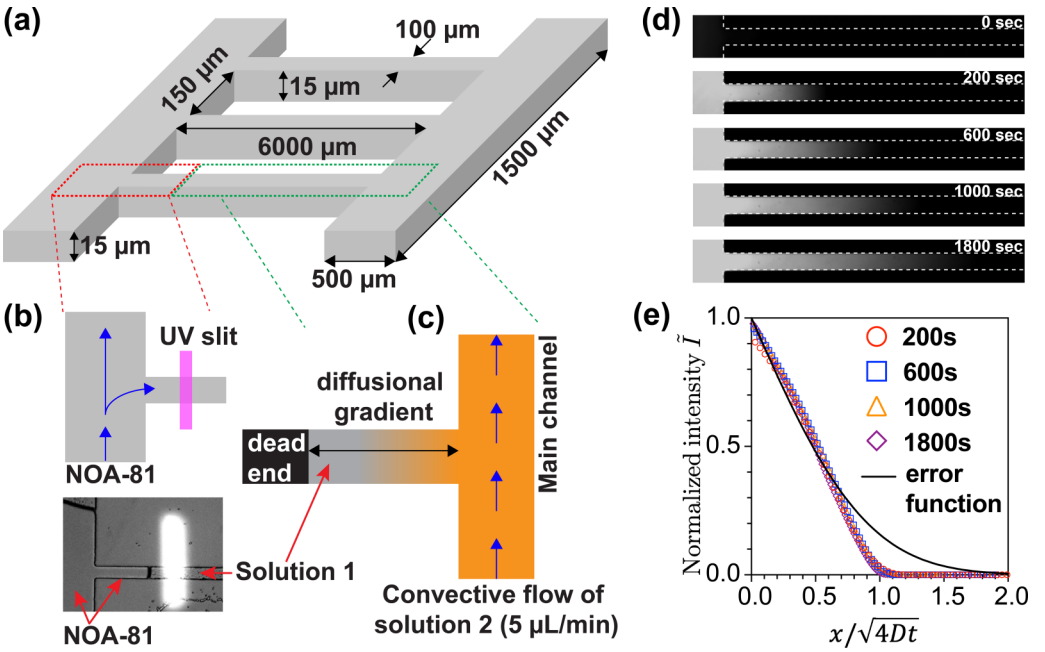

FIG. 1. Establishing transient and diffusional chemical gradients with *in situ* formed dead-end channels. (a) Design of the microfluidic device. (b) Formation of the dead-end with photopolymerization of NOA-81. (c) Concentration contrast between solution 1 and 2 establishes the transient chemical gradient. (d) Fluorescence images of fluorescein diffusing into the dead-end channel. (e) Normalized intensity profiles from panel (d) agree with the error function and confirm no significant fluid convection in the dead-end channel.

the camera is taking the picture, i.e., 175 ms every 3 min. This setup gives a total exposure time of 35 s in a 10 h experiment.

III. RESULTS AND DISCUSSION

Starting with the case of no apparent gradients [Fig. 2(a)], intensity profiles change slowly with time, indicating limited droplet transport in the dead-end channel. Abnormal peaks also appear similarly in all intensity profiles and remain near the penetration depth of flows streamlines ($x = 150\ \mu$m), regardless of the presence or type of chemical gradients. These peaks are likely caused by local accumulation of droplets due to asymmetric flow streamlines [32] near the entrance inside dead-end channels. However, this effect is not dramatic as the increase of intensity is about 10% from the main channel and remains constant during the experiment.

Next, by choosing solution 1 as CW and solution 2 as SW [Fig. 2(b)], the concentration difference in NaCl and $CaCl_2$ between CW and SW ($\Delta c_{NaCl} \approx 1.6$ M and $\Delta c_{CaCl_2} \approx 0.25$ M, [22,34]) establishes electrolyte gradients pointing into the dead-end channel. Surprisingly, the temporal change of intensity profiles in this case is not substantially different from that in Fig. 2(a). We rule out the effect of initially higher viscosity in the dead-end channel, which would quickly reduce from η_{CW} ($\approx$1.22 mPa s at 25 °C, [34]) to η_{SW} ($\approx$0.95 mPa s at 25 °C) in the droplet migration region, due to fast diffusion of ions while SW continuously flows in the main channel. Therefore, Fig. 2(b) suggests that electrolyte gradients do not drive significant DP migration at high salinity as they usually do in the low-salinity limit.

To rationalize this result, we notice that the droplet's zeta potential is very small in our system—ζ_p measured by Malvern ZetaSizer is -5 to -7 mV for droplets stabilized by 2.5 mM CBS in SW. This small ζ_p would reduce the electrostatic interaction between colloids and ion species, yielding

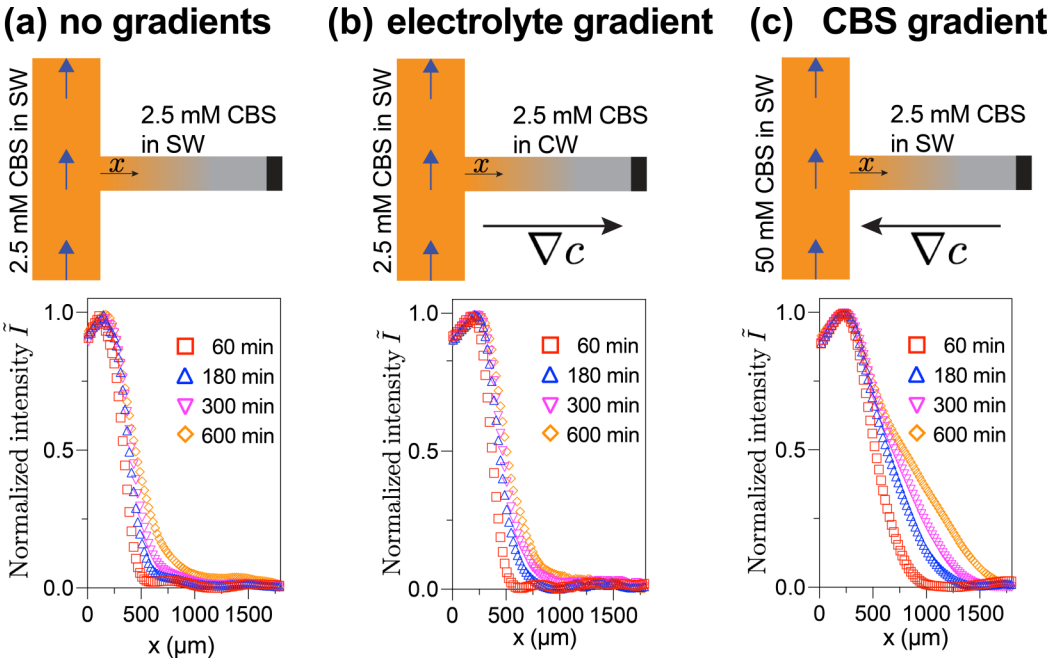

FIG. 2. Droplet migration when (a) no apparent gradients, (b) electrolyte gradient, and (c) CBS gradient are established in the dead-end channel. The top panel shows the design of solution 1 in the dead-end channel and solution 2 in the main channel for each experiment. Fluorescence intensity profiles at different time points in the dead-end channel are displayed in the bottom panel.

slow DP migration. A similar scenario could broadly exist in colloidal systems at high salinity for two reasons. First, many emulsions are stabilized by nonionic or zwitterionic surfactants to resist high salinity, where droplet's surface charge density is small by design. Second, maintaining sufficiently large ζ_p at high salinity is usually rather difficult due to the screening and neutralization of surface charges by electrolyte ions [35]. Particularly, the charge neutralization is not considered in Refs. [17,21] but likely to exist in many systems like ours involving divalent ions. In addition to small ζ_p, the grad-log scaling $U_{\mathrm{DP}} \sim \nabla c/c$ [36] suggests that a steeper electrolyte gradient (∇c) is needed at elevated c to yield DP velocity (U_{DP}) similar to that in the low-salinity limit. While mechanisms such as chemical reaction could reduce c by scavenging background electrolytes [37], they require specific chemical compositions and thus are not applicable in general systems.

From the analysis, nonelectrolyte gradients could be possible candidates to drive DP at high salinity. Such migration usually does not require charged colloids nor has the grad-log scaling with electrolyte concentration [36,38]. Specifically in our system, a CBS gradient pointing outward in the dead-end channel could be established between 50 mM (≈2% w/v) and 2.5 mM CBS [Fig. 2(c)]. Indeed, temporal changes of intensity profiles clearly indicate effective DP proceeding down the CBS gradient, which leads to enhanced droplet transport into the dead-end channel. Because CBS solution in this experiment is always above its critical micelle concentration (≈1.2 mM in 1M NaCl [39]), the difference in CBS concentration would generate micelle gradients with a relatively constant distribution of monomers [23]. Specifically, 50 mM CBS gives a micelle concentration of 0.5 mM based on the reported micelle aggregation number $N_g \approx 100$ [39], whereas the micelle concentration in 2.5 mM CBS solution is only 0.013 mM.

Given the droplet migration *down* the micelle concentration gradient, it is unlikely driven by soluto-capillary flow, which would require CBS monomer gradients [26,27,40] and induce droplet migration *up* the gradient [11]. Similarly, the solubilization interaction between micelles and

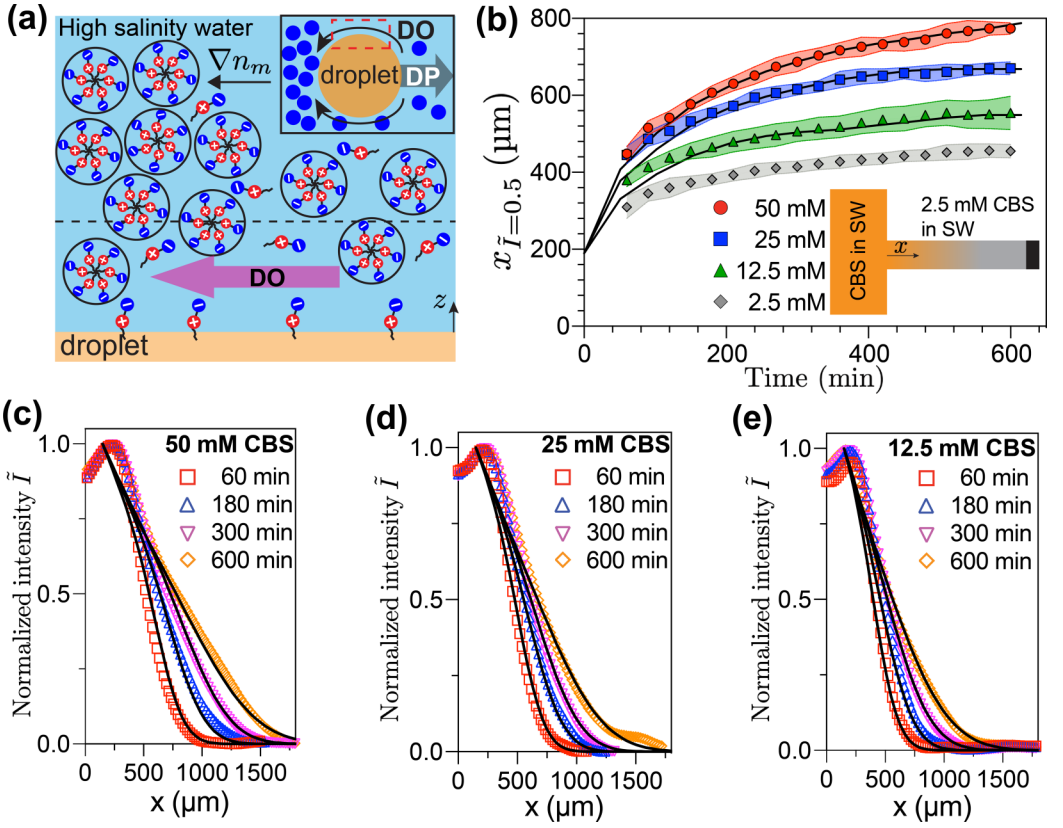

FIG. 3. Quantitative measurements of DP migration of oil droplets under CBS gradients in high-salinity solutions. (a) Repulsive interaction between droplets and micelles generates the diffusio-osmotic (DO) flow. (b) Progression of $x_{\tilde{I}=0.5}$ extracted from intensity profiles in panels (c)–(e). The shaded area in panel (b) shows the standard deviation from experiments (symbols) and solid lines are model predictions. In panels (b)–(e), symbols are experimental results and solid lines are fitting outcomes from the transport model.

droplets [28] would also drive DP *up* the surfactant gradient. Furthermore, due to the amphoteric nature of CBS and high salinity in the solution, the electrostatic interaction in our system is expected to be much weaker than that reported under ionic surfactant gradients in the low-salinity limit [15,23–25].

A generalized repulsive interaction between micelles and droplets can be inferred based on the expression of DP velocity [10,41],

$$U_{\mathrm{DP}} = -U_{\mathrm{DO}} = \frac{\nabla\mu}{\eta}\int_0^\infty z(n_m^* - n_m)dz. \tag{2}$$

In Eq. (2), z is the direction vertical to the droplet surface, η is the viscosity of the continuous phase, and $\nabla\mu = k_B T\nabla \ln n_m$ represents the chemical gradient of micelles. The integration measures the deficiency of micelles in the sublayer close to the droplet (n_m^*) compared with that in the bulk solution (n_m). Because $n_m^* < n_m$ for the repulsive interaction, the diffusio-osmotic flow (U_{DO}) is directed along the micelle gradient near the droplet surface, yielding DP migration down the CBS gradient [Fig. 3(a)].

To characterize the repulsive droplet-micelle interaction, we perform systematic measurements of DP migration under CBS gradients of different magnitudes. The migration velocity is quantified by the temporal progression of $x_{\tilde{I}=0.5}$, which is the location in dead-end channels with normalized

intensity of 0.5 [Fig. 3(b)]. Higher CBS concentration in the main channel (n_m^0) results in larger $x_{\tilde{I}=0.5}$, or deeper migration of drops into the dead-end channel. In the case of absent micelle gradients [Fig. 3(b), diamonds], $x_{\tilde{I}=0.5} \approx 450$ μm after 10 hours. After subtracting the penetration depth of flow streamlines ($L_0 \approx 150$ μm), this value (300 μm) becomes close to the droplet diffusion length x_{diff}, where $c/c_0 = 0.5$ in Eq. (1) leads to $x_{\text{diff}} \approx \sqrt{D_p t} \approx 240$ μm. $D_p \approx 1.57$ μm^2/s is estimated via the Einstein-Stokes relation using the droplet size ($r_p = 139.8 \pm 24.6$ nm, determined by dynamic light scattering, DLS) and solution viscosity ($\eta_{SW} \approx 0.95$ mPa s).

Measured intensity profiles can be modeled by solving [Figs. 3(b)–3(e)] the diffusion equation for CBS micelles in above-cmc (critical micelle concentration) solutions [42],

$$\frac{\partial n_m}{\partial t} = D_m \nabla^2 n_m, \tag{3}$$

and convection-diffusion equation for droplets

$$\frac{\partial n_p}{\partial t} + \nabla \cdot (U_p n_p) = D_p \nabla^2 n_p. \tag{4}$$

The diffusion coefficient of micelles D_m is estimated via the Einstein-Stokes relation based on size measurements from DLS ($r_m = 3.44 \pm 0.48$ nm). The convection term $U_p = U_{\text{DP}} + u_0$ in droplet transport includes DP migration $U_{\text{DP}} > 0$ and osmotic flow $u_0 < 0$ of the fluid near the channel wall, both of which are induced by micelle gradients. Although depletion forces between droplets may arise due to CBS micelles, the interaction energy is on the order of thermal energy for the low micelle volume fraction (<5%) and quickly decays once the distance between droplets exceeds r_m [43]. Therefore, droplets are considered noninteracting in this model.

First, the expression of U_{DP} depends on the interaction energy Φ between micelles and droplets. From Eq. (2),

$$\begin{aligned} U_{\text{DP}} &= \frac{k_B T}{\eta} \nabla \ln n_m \int_0^\infty n_m \left[\exp\left(\frac{-\Phi}{k_B T} \right) - 1 \right] z dz \\ &= \frac{k_B T}{\eta} N_A \nabla n_m \int_0^\infty \left[\exp\left(\frac{-\Phi}{k_B T} \right) - 1 \right] z dz, \end{aligned} \tag{5}$$

where the unit of n_m is molar concentration so the Avogadro constant N_A is included. We assume an inner region near the droplet surface $z < r_I \approx r_m$ where $\Phi \to \infty$, and an outer region $z > r_I$ where the integration in Eq. (5) depends on n_m,

$$U_{\text{DP}} = \frac{k_B T}{\eta} N_A \nabla n_m \left[-\frac{1}{2} (r_m)^2 - f(n_m) \right]. \tag{6}$$

Fitting measured intensity profiles with Eq. (6), however, is difficult because $f(n_m)$ is not known and may involve multiple fitting parameters. Therefore, we approximate it with the power law of n_m,

$$U_{\text{DP}} \approx \frac{k_B T}{\eta} N_A \nabla n_m [-A_0 (n_m)^\alpha] \tag{7}$$

where $A_0 > 0$ is the scaling constant. When $\alpha = 0$ and $A_0 = \frac{1}{2}(r_m)^2$, Eq. (7) recovers the formula derived by assuming a hard-sphere repulsion energy [36,44,45]. Our fitting results yield $\alpha \approx -0.75$ and $A_0 \approx 20$ nm^2 mM$^{0.75}$ (see Supplemental Material for details [29]), suggesting a non-negligible repulsive interaction that decays with n_m in the outer region. In addition, $A_0 (n_m)^{-0.75} > 20$ nm^2 for $n_m < 1$ mM. Thus, in Eq. (6), contribution from the outer region $f(n_m) = A_0 (n_m)^{-0.75} - \frac{1}{2}(r_m)^2 > 14$ nm^2 is more significant compared with $\frac{1}{2}(r_m)^2 = 6$ nm^2 from the inner region.

Second, the osmotic flow arises from the exclusion of micelles from the channel wall, and thus is similarly directed along the micelle gradient as U_{DO}. The effect of this flow on droplet migration is represented by the convection velocity u_0, which depends on the balance between the osmosis

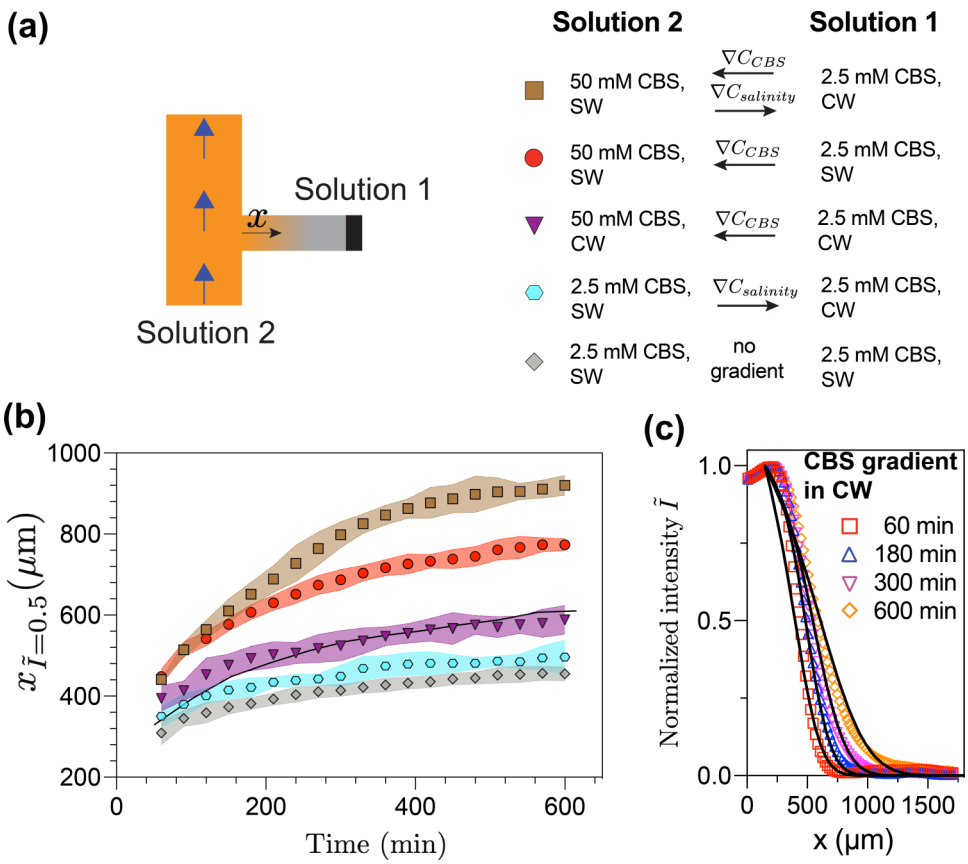

FIG. 4. (a) Design of solution 1 and 2 for establishing CBS gradients in different salinity conditions. (b) Progression of $x_{\tilde{I}=0.5}$. Diamond, hexagon, and circle symbols are the same experiments as in Figs. 2(a)–2(c), respectively. (c) Intensity profiles of droplets migration under CBS gradients in uniform CW. Model prediction is plotted in solid lines in panels (b) and (c).

and pressure-driven flow, micelle-wall interaction, and vertical distribution of droplets affected by the buoyancy (see Supplemental Material for details [29]). Due to the complexity of such factors, u_0 is treated as a fitting parameter (the other two in the model are α and A_0) that is spatially and temporally constant, accounting for the average effect of osmotic flow on droplet transport. Fitting results reveal that u_0 is smaller than 0.01 μm/s and increases with the magnitude of micelle gradients. On the other hand, this osmotic flow does not affect the diffusion of micelles, which are buoyancy-neutral and diffuse much faster than droplets (i.e., $Pe = u_0 h/D_m \ll 1$, $h = 15$ μm is the height of the channel).

So far, CBS gradients only involves homogeneous SW, whereas solutions of higher or mixed salinities exist in many systems such as geological reservoirs [46,47]. To investigate such effects on DP migration, we establish CBS gradients in two additional salinity conditions, one with uniform connate water (CW, higher salinity than SW) and the other with simultaneous salinity gradients. The design of solution 1 and 2 for these two conditions is described in Fig. 4(a) triangle and square, respectively.

Before discussing specific results of droplet migration, we first analyze the structure change of CBS micelles with salinity. In fact, DLS measurements yield $r_m^{\mathrm{SW}} \approx 3.44 \pm 0.48$ nm and $r_m^{\mathrm{CW}} \approx 10.4 \pm 1.84$ nm (including the viscosity increase), where the micelle size increases by a factor of

three with elevated salinity from SW to CW. While antipolyelectrolyte effect [48–50] has been proposed for the size increase of zwitterionic surfactant micelles, the carbon space number ($n = 3$) between positive and negative charged groups in the CBS molecule is too small to dominate the threefold increase in r_m. A more reasonable factor for larger CBS micelles in higher salinity is the increased micelle aggregation number N_g [51,52], which is utilized to explain the observation in Fig. 4(b).

Considering DP under CBS gradients in homogeneous CW [Fig. 4(b), triangles] and SW [Fig. 4(b), circles], both experiments involve no salinity gradients and the one with larger micelles [Fig. 4(b), triangles] yields slower DP migration. Such observation seems to disagree with Eq. (6) that intuitively suggests otherwise. This is because the increase in r_m triggers two opposite effects on DP migration under CBS gradients in homogeneous CW. On the one hand, assuming spherical micelles, $r_m \sim (N_g)^{1/3}$ [35] so $U_{\mathrm{DP}} \sim (N_g)^{2/3}$ by ignoring $f(n_m)$ in Eq. (6). On the other hand, given the total CBS concentration, $\nabla n_m \sim n_m^0 \sim (N_g)^{-1}$ and thus $U_{\mathrm{DP}} \sim (N_g)^{-1}$. The overall effect of such two opposing factors gives $U_{\mathrm{DP}} \sim (N_g)^{-1/3} \sim (r_m)^{-1}$, which qualitatively agrees with the observation.

We further apply the transport model to quantitatively predict the droplet migration under CBS gradients in CW. The expression of U_{DP},

$$U_{\mathrm{DP}} \approx \frac{k_B T}{\eta} N_A \nabla n_m [-A_0 (n_m)^{\alpha} - \Delta r_m], \tag{8}$$

involves the additional term $\Delta r_m = \frac{1}{2}(r_m^{\mathrm{CW}})^2 - \frac{1}{2}(r_m^{\mathrm{SW}})^2 \approx 48.6\ \mathrm{nm}^2$ to account for the increase of r_m in Eqs. (6) and (7). And fitted values of $\alpha = -0.75$, $A_0 = 20\ \mathrm{nm}^2\ \mathrm{mM}^{0.75}$, and $u_0 = 0.008\ \mu\mathrm{m/s}$ are used for calculating U_{DP}. Meanwhile, the transport of micelles in homogeneous CW also follows Eq. (3). However, their concentration in the main channel n_m^0 drops by a factor of $(r_m)^3$, assuming the size variation is mainly contributed by changes in N_g. Calculation indicates a good agreement between the model prediction [solid lines in Figs. 4(b) and 4(c)] and the experimental data [Figs. 4(b), triangles and 4(c), symbols].

By contrast, compared with CBS gradients alone in SW [Fig. 4(b), circles], additional salinity gradients [Fig. 4(b), squares] yield faster DP that enhances the delivery of droplets. In this case, the transport of CBS follows

$$\frac{\partial n_T}{\partial t} = \frac{\partial}{\partial x}\left(D_m \frac{\partial n_T}{\partial x}\right), \tag{9}$$

where $n_T = \mathrm{cmc} + N_g n_m$ is the total CBS concentration including monomers dispersed in the solution and associated in micelles [42]. Different from the migration in homogeneous SW or CW given by Eq. (3), salinity gradients produce variations of cmc and N_g, which in turn change r_m and thus D_m as micelles diffuse. To solve for n_m, additional diffusion equations for all electrolyte ions are required since their local compositions determine micelle properties in Eq. (9). More importantly, the complicated monomer-micelle-ion interaction has not reached a consensus and quantitative conclusion, making the computation of U_{DP} under simultaneous CBS and salinity gradients rather challenging.

However, even without referring to details of such dynamics, our transport model offers a qualitative understanding of the synergistic effect of salinity and micelle gradients. First, measurements of r_m^{SW} and r_m^{CW} suggest that r_m increases along the salinity gradient, and so does N_g assuming it dominates the change of r_m. Meanwhile, given $n_m^0 = 0.5$ mM at the pore mouth, the increasing N_g along the salinity reduces n_m to yield stronger ∇n_m compared with the case without salinity gradients [Fig. 4(a), circle and triangle]. Although the cmc of CBS reduces with salinity from 1.2 mM at the pore mouth [39], the resulted increase in n_m is less dramatic than the effect of increasing N_g. This is because, for droplet migration near the pore mouth, both the value and variation of cmc ($\leqslant$1.2 mM) are much smaller than n_T, which is on the same order of CBS concentration in the main channel (50 mM). Therefore, compared with CBS gradients in uniform

SW, additional salinity gradients yield larger r_m, stronger ∇n_m, and smaller n_m, all contributing to faster DP migration based on Eqs. (6) and (7).

IV. CONCLUSION

In summary, we present direct visualization and quantitative measurement of diffusiophoresis at high salinity. The negligible DP migration under electrolyte gradients is rationalized by the reduced electrostatic interaction between ions and droplets. Switching from electrolyte to nonelectrolyte gradients yields effective DP migration of droplets proceeding down CBS gradients, which is modeled by considering the repulsive micelle-droplet interaction. Notably, although electrolyte gradients alone do not effectively drive DP at high salinity, they show a synergistic effect with CBS gradients on DP migration. Putting these conditions in the context of subsurface reservoir flooding for oil recovery, salinity gradients arise when seawater is initially injected into the reservoir containing connate water, while homogeneous SW corresponds to the later stage when connate water is mostly displaced by seawater. Our results then suggest that the DP migration under zwitterionic surfactant gradients can be exploited to improve colloid delivery during different stages of reservoir flooding operations.

[1] M. M.-J. Lin and D. C. Prieve, Electromigration of latex induced by a salt gradient, J. Colloid Interface Sci. **95**, 327 (1983).

[2] J. L. Anderson, M. E. Lowell, D. C. Prieve, J. L. Anderson, J. P. Ebel, and M. E. Lowell, Motion of a particle generated by chemical gradients. Part 2. Electrolytes, J. Fluid Mech. **148**, 247 (1984).

[3] B. V. Derjaguin, S. S. Dukhin, and A. A. Korotkova, Diffusiophoresis in electrolyte solutions and its role in the mechanism of the formation of films from caoutchouc latexes by the ionic deposition method, Prog. Surf. Sci. **43**, 153 (1993).

[4] D. Velegol, A. Garg, R. Guha, A. Kar, and M. Kumar, Origins of concentration gradients for diffusiophoresis, Soft Matter **12**, 4686 (2016).

[5] D. C. Prieve, R. E. Smith, R. A. Sander, and H. L. Gerhart, Chemiphoresis: Acceleration of hydrosol deposition by ionic surface reactions, J. Colloid Interface Sci. **71**, 267 (1979).

[6] D. Florea, S. Musa, J. M. R. Huyghe, and H. M. Wyss, Long-range repulsion of colloids driven by ion exchange and diffusiophoresis, Proc. Natl. Acad. Sci. USA **111**, 6554 (2014).

[7] R. Guha, X. Shang, A. L. Zydney, D. Velegol, and M. Kumar, Diffusiophoresis contributes significantly to colloidal fouling in low salinity reverse osmosis systems, J. Membr. Sci. **479**, 67 (2015).

[8] S. Shin, O. Shardt, P. B. Warren, and H. A. Stone, Membraneless water filtration using CO_2, Nat. Commun. **8**, 1 (2017).

[9] B. Abécassis, C. Cottin-Bizonne, C. Ybert, A. Ajdari, and L. Bocquet, Osmotic manipulation of particles for microfluidic applications, New J. Phys. **11**, 075022 (2009).

[10] N. Shi, R. Nery-Azevedo, A. I. Abdel-Fattah, and T. M. Squires, Diffusiophoretic Focusing of Suspended Colloids, Phys. Rev. Lett. **117**, 258001 (2016).

[11] A. Banerjee, I. Williams, R. N. Azevedo, M. E. Helgeson, and T. M. Squires, Soluto-inertial phenomena: Designing long-range, long-lasting, surface-specific interactions in suspensions, Proc. Natl. Acad. Sci. USA **113**, 8612 (2016).

[12] S. Shin, E. Um, B. Sabass, J. Ault, P. Warren, and H. A. Stone, Size-dependent control of colloid transport via solute gradients in dead-end channels, Proc. Natl. Acad. Sci. **113**, 257 (2015).

[13] A. Kar, T.-Y. Chiang, I. Ortiz Rivera, A. Sen, and D. Velegol, Enhanced transport into and out of dead-end pores., ACS Nano **9**, 746 (2015).

[14] S. Marbach and L. Bocquet, Osmosis, from molecular insights to large-scale applications, Chem. Soc. Rev. **48**, 3102 (2019).

[15] S. Shin, P. B. Warren, and H. A. Stone, Cleaning by Surfactant Gradients: Particulate Removal from Porous Materials and the Significance of Rinsing in Laundry Detergency, Phys. Rev. Appl. **9**, 3 (2018).

[16] A. Garg, C. A. Cartier, K. J. Bishop, and D. Velegol, Particle zeta potentials remain finite in saturated salt solutions, Langmuir **32**, 11837 (2016).
[17] D. C. Prieve, S. M. Malone, A. S. Khair, R. F. Stout, and M. Y. Kanj, Diffusiophoresis of charged colloidal particles in the limit of very high salinity, Proc. Natl. Acad. Sci. USA **116**, 18257 (2019).
[18] R. Greene, W. Timms, P. Rengasamy, M. Arshad, and R. Cresswell, Soil and aquifer salinization: Toward an integrated approach for salinity management of groundwater, in *Integrated Groundwater Management: Concepts, Approaches and Challenges*, edited by A. J. Jakeman, O. Barreteau, R. J. Hunt, J. D. Rinaudo, and A. Ross (Springer, Cham, 2016).
[19] S. Marbach, H. Yoshida, and L. Bocquet, Osmotic and diffusio-osmotic flow generation at high solute concentration. I. Mechanical approaches, J. Chem. Phys. **146**, 194701 (2017).
[20] H. Yoshida, S. Marbach, and L. Bocquet, Osmotic and diffusio-osmotic flow generation at high solute concentration. II. Molecular dynamics simulations, J. Chem. Phys. **146**, 194702 (2017).
[21] R. F. Stout and A. S. Khair, Influence of ion sterics on diffusiophoresis and electrophoresis in concentrated electrolytes, Phys. Rev. Fluids **2**, 014201 (2017).
[22] A. Gizzatov, A. Mashat, D. Kosynkin, N. Alhazza, A. Kmetz, S. L. Eichmann, and A. I. Abdel-Fattah, Nanofluid of petroleum sulfonate nanocapsules for enhanced oil recovery in high-temperature and high-salinity reservoirs, Energy Fuels **33**, 11567 (2019).
[23] R. Nery-Azevedo, A. Banerjee, and T. M. Squires, Diffusiophoresis in ionic surfactant gradients, Langmuir **33**, 9694 (2017).
[24] P. B. Warren, S. Shin, and H. A. Stone, Diffusiophoresis in ionic surfactants: Effect of micelle formation, Soft Matter **15**, 278 (2019).
[25] V. S. Doan, P. Saingam, T. Yan, and S. Shin, A trace amount of surfactants enables diffusiophoretic swimming of bacteria, ACS Nano **14**, 14219 (2020).
[26] V. G. Levich and V. S. Krylov, Surface-tension-driven phenomena, Annu. Rev. Fluid Mech. **1**, 293 (1969).
[27] V. G. E. Levich and A. M. Kuznetsov, Motion of drops in liquids under the influence of surface-active substances, Dokl. Akad. Nauk SSSR, **146**, 145, (1962).
[28] C. Jin, C. Krüger, and C. C. Maass, Chemotaxis and autochemotaxis of self-propelling droplet swimmers., Proc. Natl. Acad. Sci. USA **114**, 5089 (2017).
[29] See Supplemental Material at http://link.aps.org/supplemental/10.1103/PhysRevFluids.6.053103 for fabrication and operation details of the microfluidic device [53–55], preparation and characterization of chemicals including emulsions, synthetic seawater (SW) [22], and connate water (CW) [34], acquisition and analysis of intensity images, fitting measured intensity profiles with the transport model, and discussion of the effect of osmotic flow on droplet migration [12].
[30] R. B. Bird, W. E. Stewart, and E. N. Lightfoot, *Transport Phenomena*, Revised 2nd ed. (John Wiley & Sons, Inc., New York, 2006).
[31] Z. Petrášek and P. Schwille, Precise measurement of diffusion coefficients using scanning fluorescence correlation spectroscopy, Biophys. J. **94**, 1437 (2008).
[32] S. Battat, J. T. Ault, S. Shin, S. Khodaparast, and H. A. Stone, Particle entrainment in dead-end pores by diffusiophoresis, Soft Matter **15**, 3879 (2019).
[33] J. L. Mynar, A. P. Goodwin, J. A. Cohen, Y. Ma, G. R. Fleming, and J. M. Fréchet, Two-photon degradable supramolecular assemblies of linear-dendritic copolymers, Chem. Commun. **20**, 2081 (2007).
[34] A. M. Shehata and H. A. Nasr El-Din, Spontaneous imbibition study: Effect of connate water composition on low-salinity waterflooding in sandstone reservoirs, in *SPE Western Regional Meeting 2015: Old Horizons, New Horizons Through Enabling Technology* (Society of Petroleum Engineers, Garden Grove, CA, 2015).
[35] J. Israelachvili, *Intermolecular and Surface Forces* (Academic Press, San Diego, CA, 2011).
[36] J. Anderson, Colloid transport by interfacial forces, Annu. Rev. Fluid Mech. **21**, 61 (1989).
[37] A. Banerjee and T. M. Squires, Long-range, selective, on-demand suspension interactions: Combining and triggering soluto-inertial beacons, Sci. Adv. **5**, eaax1893 (2019).
[38] J. L. Anderson, M. E. Lowell, and D. C. Prieve, Motion of a particle generated by chemical gradients Part 1. Non-electrolytes, J. Fluid Mech. **117**, 107 (1982).

[39] J. Wang, O. Morales-Collazo, and A. Wei, Micellization and single-particle encapsulation with dimethylammoniopropyl sulfobetaines, ACS Omega **2**, 1287 (2017).
[40] V. G. Levich and S. Technica, *Physicochemical Hydrodynamics* (Prentice-Hall, Englewood Cliffs, NJ, 1962), Vol. 689.
[41] T. M. Squires, Particles in Electric Fields, in *Fluids, Colloids, Soft Materials, and an Introduction to Soft Matter Physics*, edited by A. Fernandez-Nieves and A. Puertas (John Wiley & Sons, Inc, Hoboken, 2016).
[42] R. M. Weinheimer, D. F. Evans, and E. L. Cussler, Diffusion in surfactant solutions, J. Colloid Interface Sci. **80**, 357 (1981).
[43] J. C. Crocker, J. A. Matteo, A. D. Dinsmore, and A. G. Yodh, Entropic Attraction and Repulsion in Binary Colloids Probed With a Line Optical Tweezer, Phys. Rev. Lett. **82**, 4352 (1999).
[44] P. O. Staffeld and J. A. Quinn, Diffusion-induced banding of colloid particles via diffusiophoresis. 2. non-electrolytes, J. Colloid Interface Sci. **130**, 88 (1989).
[45] J. T. Ault, S. Shin, and H. A. Stone, Characterization of surface-solute interactions by diffusioosmosis, Soft Matter **15**, 1582 (2019).
[46] S. B. Fredriksen, A. U. Rognmo, and M. A. Fernø, Pore-scale mechanisms during low salinity waterflooding: Oil mobilization by diffusion and osmosis, J. Pet. Sci. Eng. **163**, 650 (2018).
[47] A. Katende and F. Sagala, A critical review of low salinity water flooding: Mechanism, laboratory and field application, J. Mol. Liq. **278**, 627 (2019).
[48] F. Wang, J. Yang, and J. Zhao, Understanding anti-polyelectrolyte behavior of a well-defined polyzwitterion at the single-chain level, Polym. Int. **64**, 999 (2015).
[49] G. S. Georgiev, E. B. Kamenska, E. D. Vassileva, I. P. Kamenova, V. T. Georgieva, S. B. Iliev, and I. A. Ivanov, Self-assembly, antipolyelectrolyte effect, nonbiofouling properties of polyzwitterions, Biomacromolecules **7**, 1329 (2006).
[50] V. Carbon and Y. Chevalier, Aqueous solutions of zwitterionic surfactants with, Langmuir **12**, 3225 (1996).
[51] X.-Z. Ren, G.-Z. Li, H.-L. Wang, and X.-H. Xu, A study of betaine solutions by fluorescent probes of pyrene and pyrene-3-carboxaldehyde, Colloids Surf., A **100**, 165 (1995).
[52] A. P. Gerola, P. F. Costa, F. Nome, and F. Quina, Micellization and adsorption of zwitterionic surfactants at the air/water interface, Curr. Opin. Colloid Interface Sci. **32**, 48 (2017).
[53] J. S. Paustian, C. D. Angulo, R. Nery-Azevedo, N. Shi, A. I. Abdel-Fattah, and T. M. Squires, Direct measurements of colloidal solvophoresis under imposed solvent and solute gradients, Langmuir **31**, 4402 (2015).
[54] Y. Xia and G. M. Whitesides, Soft lithography, Annu. Rev. Mater. Sci. **28**, 153 (1998).
[55] D. Bartolo, G. Degré, P. Nghe, and V. Studer, Microfluidic stickers, Lab Chip **8**, 274 (2008).